Geophysical Journal International

Geophys. J. Int. (2011) **186,** 1078–1094 doi: 10.1111/j.1365-246X.2011.05112.x

Hydrogeology of Stromboli volcano, Aeolian Islands (Italy) from the interpretation of resistivity tomograms, self-potential, soil temperature and soil CO_2 concentration measurements

A. Revil,[1,2] A. Finizola,[3] T. Ricci,[4] E. Delcher,[3] A. Peltier,[5] S. Barde-Cabusson,[6] G. Avard,[7] T. Bailly,[8] L. Bennati,[9] S. Byrdina,[2] J. Colonge,[8] F. Di Gangi,[10] G. Douillet,[11] M. Lupi,[12] J. Letort[8] and E. Tsang Hin Sun[8]

[1] *Colorado School of Mines, Department of Geophysics, Golden, CO* 80401, *USA. E-mail: arevil@mines.edu*
[2] *ISTerre, CNRS, UMR* 5559, *Université de Savoie, Equipe Volcan, Le Bourget du Lac, France*
[3] *Laboratoire GéoSciences Réunion, Université de la Réunion, Institut de Physique du Globe de Paris, Sorbonne Paris-Cité, CNRS UMR* 7154, *15 rue René Cassin,* 97715 *Saint-Denis cedex 9, La Réunion, Indian Ocean, France*
[4] *Istituto Nazionale di Geofisica e Vulcanologia, Roma, Italy*
[5] *Institut de Physique du Globe de Paris et Université Paris Diderot, Sorbonne Paris-Cité, CNRS UMR* 7154, *Paris, France*
[6] *Institute of Earth Sciences Jaume Almera, Consejo Superior de Investigaciones Científicas, Spain*
[7] *Observatorio Vulcanológico y Sismológico de Costa Rica, Costa Rica*
[8] *Ecole et Observatoire des Sciences de la Terre, Université de Strasbourg, France*
[9] *Earth and Atmospheric Sciences Department, Purdue University, West Lafayette, IN, USA*
[10] *Istituto Nazionale di Geofisica e Vulcanologia, Palermo, Italy*
[11] *Ludwig Maximilians Universitaet, Munich, Germany*
[12] *University of Bonn, Steinmann Institute, Geodynamics / Geophysics, Germany*

Accepted 2011 June 11. Received 2011 June 9; in original form 2011 February 9

SUMMARY

To gain a better insight of the hydrogeology and the location of the main tectonic faults of Stromboli volcano in Italy, we collected electrical resistivity measurements, soil CO_2 concentrations, temperature and self-potential measurements along two profiles. These two profiles started at the village of Ginostra in the southwest part of the island. The first profile (4.8 km in length) ended up at the village of Scari in the north east part of the volcano and the second one (3.5 km in length) at Forgia Vecchia beach, in the eastern part of the island. These data were used to provide insights regarding the position of shallow aquifers and the extension of the hydrothermal system. This large-scale study is complemented by two high-resolution studies, one at the Pizzo area (near the active vents) and one at Rina Grande where flank collapse areas can be observed. The Pizzo corresponds to one of the main degassing structure of the hydrothermal system. The main degassing area is localized along a higher permeability area corresponding to the head of the gliding plane of the Rina Grande sector collapse. We found that the self-potential data reveal the position of an aquifer above the villages of Scari and San Vincenzo. We provide an estimate of the depth of this aquifer from these data. The lateral extension of the hydrothermal system (resistivity ∼15–60 ohm m) is broader than anticipated extending in the direction of the villages of Scari and San Vincenzo (in agreement with temperature data recorded in shallow wells). The lateral extension of the hydrothermal system reaches the lower third of the Rina Grande sector collapse area in the eastern part of the island. The hydrothermal body in this area is blocked by an old collapse boundary. This position of the hydrothermal body is consistent with low values of the magnetization ($<$2.5 A m^{-1}) from previously published work. The presence of the hydrothermal body below Rina Grande raises questions about the mechanical stability of this flank of the edifice.

Keywords: Tomography; Electrical properties; Hydrogeophysics; Volcano monitoring.

1 INTRODUCTION

The localization of hydrothermal systems and aquifers in active volcanoes is a fundamental step in assessing several geological hazards like phreatic explosions, phreato-magmatic eruptions, and flank collapses (Petrinovic & Piñol 2006; Lorenz & Kurszlaukis 2007; Weinstein 2007). Phreatic explosions are bursts of confined pockets of steam and gas with no direct involvement of magma,

apart from the source of the steam and of the involvement or not of juvenile fluids (Barberi *et al*. 1993). Phreatomagmatic eruptions can occur when water encounters a magmatic body (Barberi *et al.* 1992). Hydrothermal systems can also produce, by long-lived alteration, mechanically weakened rocks and be responsible for the collapse of the flanks of volcanic edifices (López & Williams 1993; Aizawa *et al*. 2009). In the case of volcanic islands, such giant landslides can in turn generate tsunamis. Stromboli is a prime example (Tinti *et al*. 1999, 2000, 2003, 2006, 2008; Tibaldi 2001; Bonaccorso *et al*. 2003; Apuani *et al*. 2005; Romagnoli *et al*. 2009a, b). The localization of aquifers is also important because water is a scarce resource in some volcanic areas and the supply of fresh water is increasingly becoming a problem as the population and tourism increase (Cruz & França 2006).

In hydrogeology, the presence of aquifers is usually detected by drilling. An estimate of hydraulic conductivity can be obtained by pumping or slug tests and hydraulic tomography (Carrera *et al*. 2005; Cardiff *et al*. 2009). However, drilling a set of boreholes in volcanic formations can be very expensive and a difficult task due to steep topography and the mechanical resistance of some volcanic rocks. Geophysical methods represent a non-intrusive approach to handling this problem. Traditionally, electromagnetic methods (especially the audiomagnetotelluric and time-domain electromagnetic methods) have been used to look for aquifers in active volcanoes (e.g. Fitterman *et al*. 1988; Krivochieva & Chouteau 2003; Aizawa *et al*. 2005; Aizawa *et al*. 2009). This is because electrical resistivity is sensitive to the water content of rocks. Unfortunately electrical resistivity is also known to be affected by the presence of clays and zeolites through their cation exchange capacity (Waxman & Smits 1968; Revil *et al*. 2002; Coppo *et al*. 2008). Salinity of the pore water and temperature are two other parameters influencing the resistivity of porous rocks (Waxman & Smits 1968; Revil *et al*. 1998; Revil 1999). Therefore, electromagnetic methods cannot be used as stand-alone methods to determine the presence of aquifers and the extension of the hydrothermal system in volcanic areas. Also electromagnetic methods have a limited spatial resolution, at least with the number of data currently obtained over volcanic areas and existing algorithms.

In this paper, we show that the combination of self-potential data, large scale DC-resistivity tomography, and measurements of soil temperature and soil CO_2 concentrations and fluxes can be used to assess the extent of the hydrothermal system and the presence of aquifers at the scale of a volcanic edifice. The resistivity measurements were performed using an unusually long resistivity cable (16 wires, 2.5 km in length). Such a cable offers a strong advantage regarding the acquisition time with respect to classical acquisition measurements using two cables for dipole–dipole measurements with a generator and a voltmeter. Stromboli, an active volcanic located in the Aeolian Archipelago in Italy, is a suitable natural laboratory to test these methods because of the accessibility of the volcano, its strong volcanic activity, and the relatively small dimensions of its emerged part. We present new field results to determine the extent of the hydrothermal system and the presence of aquifers at the scale of this island using the combination of the methods mentioned above.

2 TECTONIC SETTING AND HISTORICAL VOLCANIC ACTIVITY

Stromboli is a stratovolcano corresponding to the northernmost island of the Aeolian volcanic arc in the Southern Tyrrhenian sea

Figure 1. Geographical location of Stromboli Island. (a) The inset shows the position of the Aeolian Archipelago in the Tyrrhenian Sea. (b) Close-up of the northern coast of Sicily showing the seven main islands (Alicudi, Filicudi, Salina, Lipari, Panarea, Stromboli and Vulcano) of the Aeolian archipelago. (c) Picture of Stromboli island (by A. Finizola, taken in 1999) showing the Sciara del Fuoco collapse structure.

(Fig. 1). It rises from a depth of 2000 m below sea level (b.s.l.) to an elevation of 924 m a.s.l. (metres above sea level) (see Segre 1968; Romagnoli *et al*. 2009a, b). It is one of the four active volcanic islands (with Vulcano, Lipari and Panarea) of the Aeolian archipelago, whose existence is related to the subduction of the African plate under the Eurasian plate (Barberi *et al*. 1974). Geological surveys (Rosi 1980; Francalanci 1987; Keller *et al*. 1993) showed that the subaerial part of the volcanic cone was built up during the last 100 ka. The formation of the emerged part of the edifice can be divided into seven discrete eruptive phases separated by erosional deposits and / or by collapses of calderas and flanks (Pasquarè *et al.* 1993). Defining these phases will be important to interpreting the geophysical data.

The first phase corresponds to PaleoStromboli I between ∼85 and 64 ka ago. At the end of PaleoStromboli I, a large caldera depression formed at the top of the volcano. The boundary of this caldera is denoted as PST I in Fig. 2. The second phase corresponds to PaleoStromboli II ended with an erosional phase. The third phase corresponds to PaleoStromboli III during which a large summit caldera developed ∼34 ka ago (see PST III in Fig. 2). The fourth phase is related with Scari units ending with strong phreatomagmatic events and the formation of the large Scari caldera ∼26 ka ago (Nappi *et al*. 1999; Gillot & Keller 1993). These two depressions PST III and Scari calderas were filled with lava flows of lower Vancori units which represent the fifth phase ended ∼ 13 ka ago (Gillot 1984). The formation of NeoStromboli crater occurred about 13 ka ago and constitutes the beginning of the sixth phase (Hornig-Kjarsgaard *et al.* 1993). Neo-Stromboli period is characterized by a large amount of lava flows, especially to the northwest of the edifice. Four onshore parasitic centers can be identified for the Neo-Stromboli period including (i) Timpone del Fuoco (North of

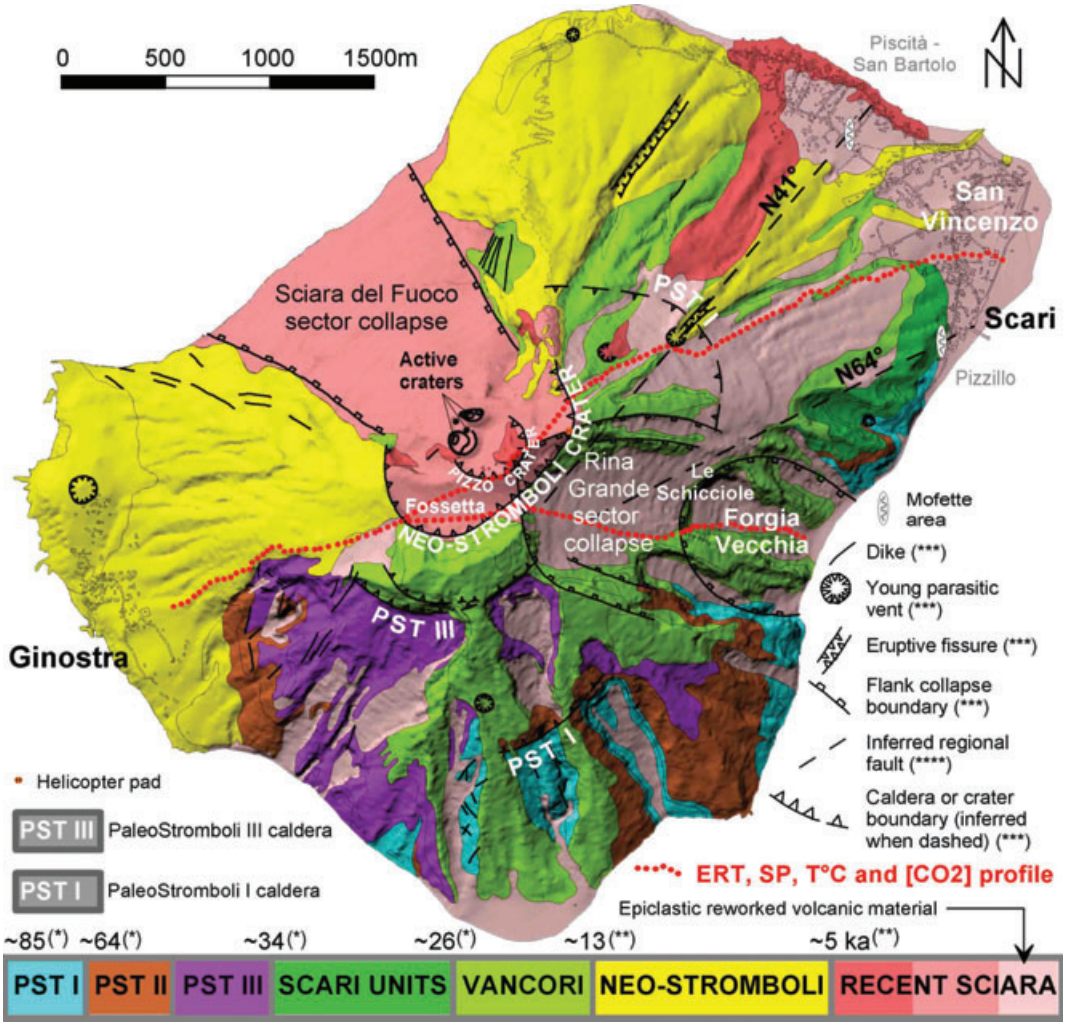

Figure 2. Geological map of Stromboli volcano (modified from Keller *et al.* 1993; Finizola *et al.* 2006). The red points indicate the positions of the measurements along the two profiles: (1) Ginostra-Scari and (2) Ginostra-Forgia Vecchia. *From Gillot & Keller (1993), **From Gillot (1984), ***From Keller *et al*. (1993), ****From Finizola *et al*. (2002).

Ginostra), (ii) Vallonazzo (eruptive fissure, NE), (iii) Punta Labronzo (eccentric center, North) and (iv) Nel Cannestrá (eruptive fissure, NE) (see their position in Fig. 2).

The transition between the NeoStromboli and the recent Stromboli cycle (seventh phase) occurred approximately 5 ka ago (Gillot & Keller 1993). During this period, the eastern aerial flank of Stromboli has been affected by several major collapses. The oldest one located in the Eastern part of the island, Le Schicciole (see position in Fig. 2), involved the PaleoStromboli units. These events have caused the horseshoe-shaped structures of (i) the Sciara del Fuoco (5 ka ago, Hornig-Kjarsgaard *et al*. 1993) and (ii) the Rina Grande area (Fig. 2). The latter cut the Vancori basaltic units in the northern and southern part of the collapse structure and affected partially the boundary of NeoStromboli crater in the upper part of the collapse structure, reaching with the top of the collapse structure the Pizzo summit area.

3 FIELD SURVEY

A large-scale survey was performed in 2011 January during a 2-week period. Electrical resistivity measurements were obtained using a set of 64 stainless steel electrodes, a set of 16 reels (four take-out per reel, one every 40 m) and the ABEM Terrameter SAS-4000 impedancemeter. The contact of the electrodes with the ground was improved by adding salty water and bentonite. For 95 per cent of the measurements, the contact resistance of the electrodes with the ground was between 0.5 and 3 kohm. Getting such low contact resistances were required to inject a 200 mA current into the ground, a value necessary to get measurements with high signal-to-noise ratios. The duration of the current injection was 1 s with 0.5 s between injections. It is important to note that a previous mission with the same equipment was performed in 2009 May but failed due to the very dry soil conditions. This explains why a second mission was planned in winter (December and January are indeed the two months with the highest rain falls at Stromboli volcano).

The first profile (5 km in length) starts at Ginostra, crosses the Pizzo area (at 918 m a.s.l.) and reaches the San Vincenzo village (near the Scari harbor) on the other side of the island (Fig. 2). The second profile (3.7 km in length) starts from the village of Ginostra, crosses the Fossetta from the Portella di Ginostra to the Portella delle croci, and goes through Rina Grande and Le Schicciole areas ending 50 m before the Forgia Vecchia shore (Fig. 2). As the total length of the cable is 2.52 km (63 spacings between 64 electrodes with 40 m spacing between take-outs), 'roll-overs' of the electrodes were

required to realize the desired profile lengths. Profile 1 consisted of two roll-along of eight reels and Profile 2 consisted of one roll-along of seven reels. The use of such a very long resistivity cable is not usual (see Gélis *et al*. 2010 for a discussion).

Acquisitions were performed with the Wenner array because of its good signal-to-noise ratio. We tried the Wenner–Schlumberger array as well and the dipole-dipole array but the results were less satisfactory than with the Wenner array and a lower signal-to-noise ratio with these arrays were requiring a higher and prohibitive number of stacks in the field (acquisition time >10 hr). This would have implied a longer duration for the acquisition despite the multichannel capability of the ABEM Terrameter SAS-4000 resistivimeter. Topographic information was included in the apparent resistivity data files. The topography was obtained from a Digital Elevation Map (DEM, Marsella *et al*. 2009) with a precision of 0.5 m in elevation and the X and Y coordinates were determined in the field using a Garmin GPS with a precision of 3 m.

In addition to 2-D DC-resistivity tomography, we acquired self-potential, soil CO_2 concentration and temperature measurements. These measurements were obtained with a spacing of 20 m along the two profiles.

Self-potential measurements were performed using a pair of non-polarizing $Cu/CuSO_4$ electrodes. The difference of electrical potential between the reference electrode (arbitrarily placed at the beginning of the profiles in Ginostra) and the moving electrode was measured with a high-impedance voltmeter with a sensitivity of 0.1 mV and a cable of 300 m. The impedance of the ground was always at least 300 times below the internal impedance of the voltmeter ($\sim$60 Mohm, so $<$200 kohm), an important point in assessing the validity of the measurements. At each station, a small hole ($\sim$10 cm deep) was dug to improve the electrical contact between the electrode and the ground. The choice of the reference position for the whole profile is arbitrary but taken near the sea in the present case. The sea is indeed considered to be a good electrical equipotential because of the high conductivity of the sea water (see Corwin & Hoover 1979).

In the field, it is possible to measure the concentration of CO_2 in the soil or its flux from the soil. Etiope *et al*. (1999) demonstrated that a linear relationship exists between ground concentrations and flux concentration values for concentrations in the range 0.1 to $\sim$ 12 per cent. For higher values, up to 100 per cent (like at Stromboli), the correlation is however expected to be poor. On Stromboli volcano, the good correlation between CO_2 concentration and CO_2 flux were shown along the entire island (see Finizola *et al*. 2006) or in the summit (Fossa) area by the comparison between the CO_2 anomalies evidenced through the flux measurement by Carapezza & Federico 2000, and the soil concentration technique by Finizola *et al*. 2003). Along the two profiles, we decided to measure only the CO_2 concentrations. To get reliable data of CO_2 concentrations, the soil gas was first sampled through a copper tube (2 mm in diameter). This copper tube was first inserted in the soil to a depth of 0.5 m. The gas was analysed directly in the field by infrared spectrometry (Edinburgh Instruments, model GasCheck). The analytical uncertainty was 5 per cent of the concentration value.

Temperature measurements at 30 cm depth were performed with thermal probes and a digital thermometer (Comark, model KM221). Readings were taken to a tenth of degree. Each temperature measurement was taken using the following procedure: (1) a small hole was dug to a depth of 30 ± 1 cm with a steel rod, 2 cm in diameter. (2) Then, we inserted a thermal probe into the hole at the depth of 30 ± 1 cm by means of a wooden stick. (3) We compacted the soil around the position of the probe. (4) Finally, a temperature reading was taken after 10–15 min. This time was required in order to achieve thermal equilibrium.

In addition to the data acquired in 2011 January along the two profiles crossing the island, we also used in this work the self-potential, soil temperature, CO_2 concentration and CO_2 flux measurements performed in 2006 May in the summit area of Pizzo. These data were collected along eight parallel linear profiles, with spacing between the measurement points along each profile of 2.5 m and distance between the profiles of 20 m. Only the CO_2 flux of this data set were already published before (Carapezza *et al*. 2009).

4 INVERSION OF THE RESISTIVITY DATA

For each acquisition, the data were inverted by means of the commercial package RES2DINV (Loke & Barker 1996) using a finite element grid for the forward modelling of the voltage response to current injection. RES2DINV is based on a finite element (non-linear) forward operator used to compute the predicted electrostatic potential distribution $\mathbf{d}_\mathrm{p}$ for a given resistivity model $\mathrm{m} : \mathrm{d_p} = K(\mathrm{m})$. An estimated model can be retrieved from the data using the inverse operator $K^{-1} : \mathrm{m}_e = K^{-1}(\mathrm{d}_0)$ where $\mathbf{m}_\mathrm{e}$ is the estimated resistivity model based on the observed electrostatic potential distribution $\mathbf{d}_0$. RES2DINV is based on a Gauss–Newton approach with a L_2 norm data misfit function. For each acquired measurement, we perform stacking to get a standard deviation better than 5 per cent with a maximum of 10 stacks (the duration of a typical acquisition was 3 hr). Data quality is therefore included in the inversion process.

Resistivity tomograms are shown in Figs 3 and 4 at iteration #5 for which a good convergence has been reached. Indeed, the rms error is 16 per cent for the profile Ginostra-Scari and 15 per cent for the profile Ginostra-Forgia Vecchia. The high rms values are due to the noise in the acquired data but as long as this noise is randomly distributed, the inversion is very robust to this noise (see discussion and numerical tests in Revil *et al.* 2008). The colour code used for the resistivity tomograms is the standard code used in DC-resistivity tomography (blue for low resistivities and red for high resistivities).

The inverted resistivities typically range from 15 to 2000–3000 ohm m. At Stromboli, a resistivity of 15 ohm m is typical of the hydrothermal system (Revil *et al*. 2004b; Finizola *et al*. 2006) and values in the range 2000–3000 ohm m correspond to basaltic lava flows (especially those associated with the Vancori or older Units discussed in Section 2 and shown in Fig. 2). The interpretation of these tomograms is provided in Figs 5 and 6. Overinterpretation of resistivity tomograms is easy. To reduce the occurrence of pitfalls, the interpretation of these tomograms has been performed carefully using the geological map and the other available CO_2, self-potential, and temperature measurements. Interpretation of these data is discussed in detail in the next section.

5 INTERPRETATION OF THE PROFILES

5.1 Profile Ginostra-Scari and Pizzo area

The resistivity tomogram presented in Fig. 3 highlights a conductive body (resistivity below 50 ohm m) in the central part of the volcano, intercepting the ground surface in the Pizzo area. It is associated with a thermal anomaly (temperature >80 °C, Fig. 3) and with an elevated CO_2 concentration close to saturation: 100 per cent of CO_2 (see 'H' in Fig. 3). In this area a positive self-potential anomaly is also recorded (Fig. 3). Such positive self-potential anomalies are

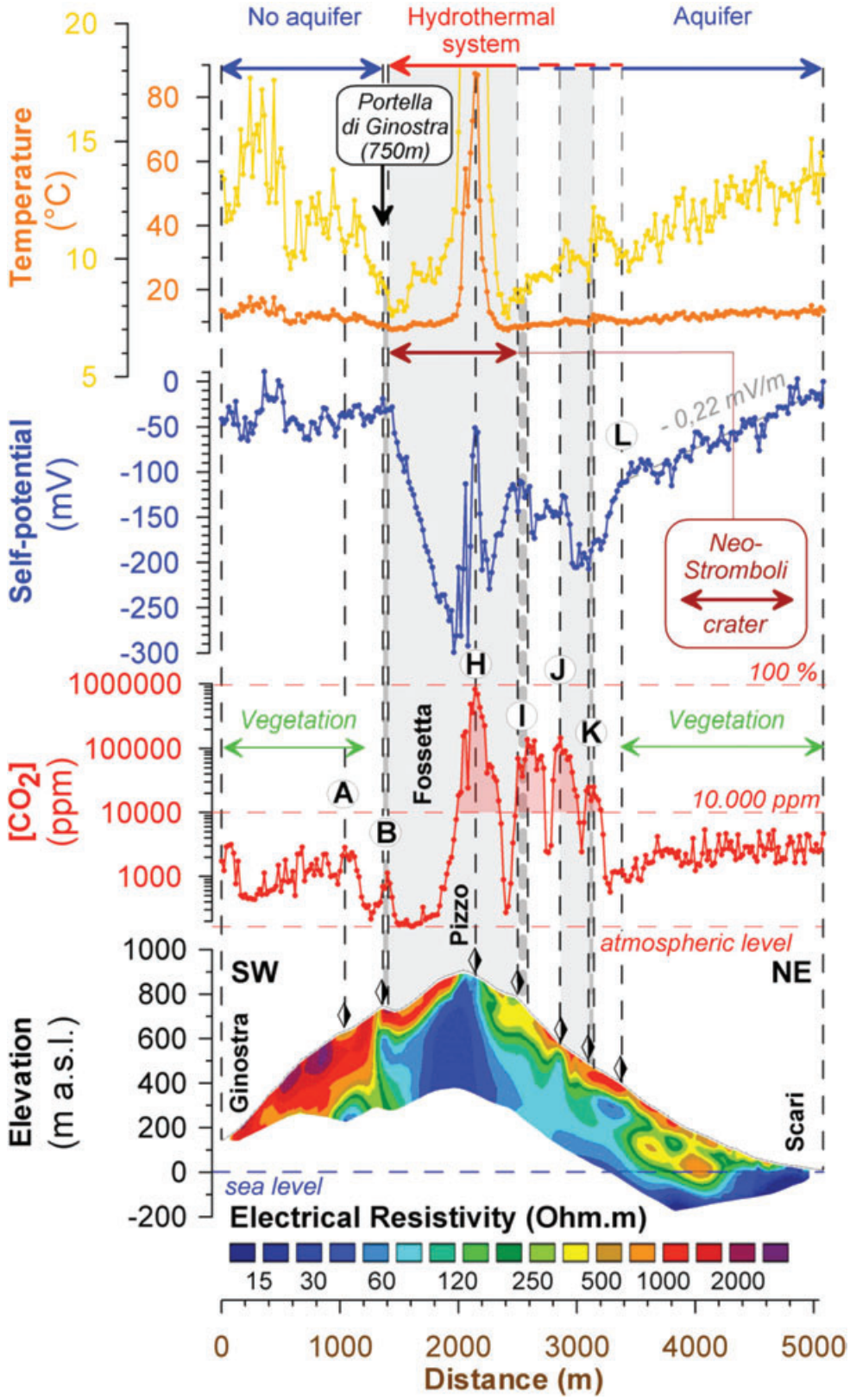

Figure 3. Temperature (°C), self-potential (in mV), soil CO_2 concentration (in ppm) measurements and DC resistivity tomogram from RES2DINV (in ohm m) along the profile Ginostra-Scari. Resistivity tomogram: vertical scaling factor 1.7, rms error 16 per cent at iteration 5 using a Gauss–Newton algorithm. Note the asymmetry in both the self-potential profile and resistivity tomogram between the SW and NE sections; the extension of the hydrothermal system is well delimited to the SW and opened to the NE. The positive self-potential anomalies at ∼2200 m along the profile are associated with a CO_2 degassing structure and temperature anomaly. Note the two scales used for the temperature data in order to show the significant fluctuations (in the range 5–20 °C) outside the area characterized by the highest temperatures. A to L represents tectonic boundaries discussed in the main text.

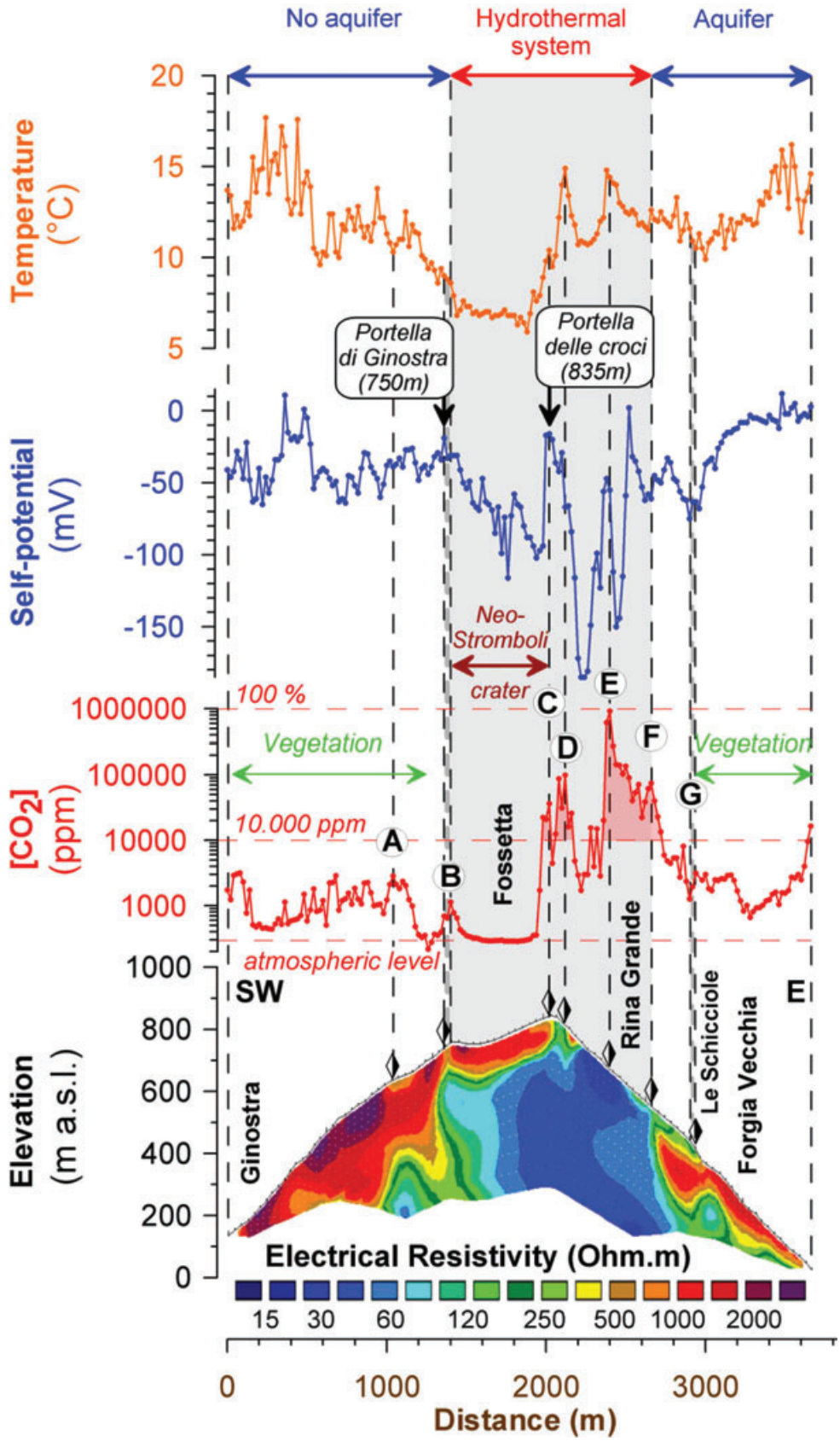

Figure 4. Temperature (°C), self-potential (in mV), soil CO_2 concentration (in ppm) measurements and DC resistivity tomogram from RES2DINV (in ohm m) along the profile Ginostra-Forgia Vecchia. Vertical scaling factor for the resistivity inverted section 1.7. RMS error 15 per cent at iteration 5 using a Gauss–Newton algorithm. Note the asymmetry in both the self-potential profile and resistivity tomogram between the SW and E sections. Note that the positive self-potential anomalies are associated with CO_2 degassing structures. A to G represents tectonic boundaries discussed in the main text.

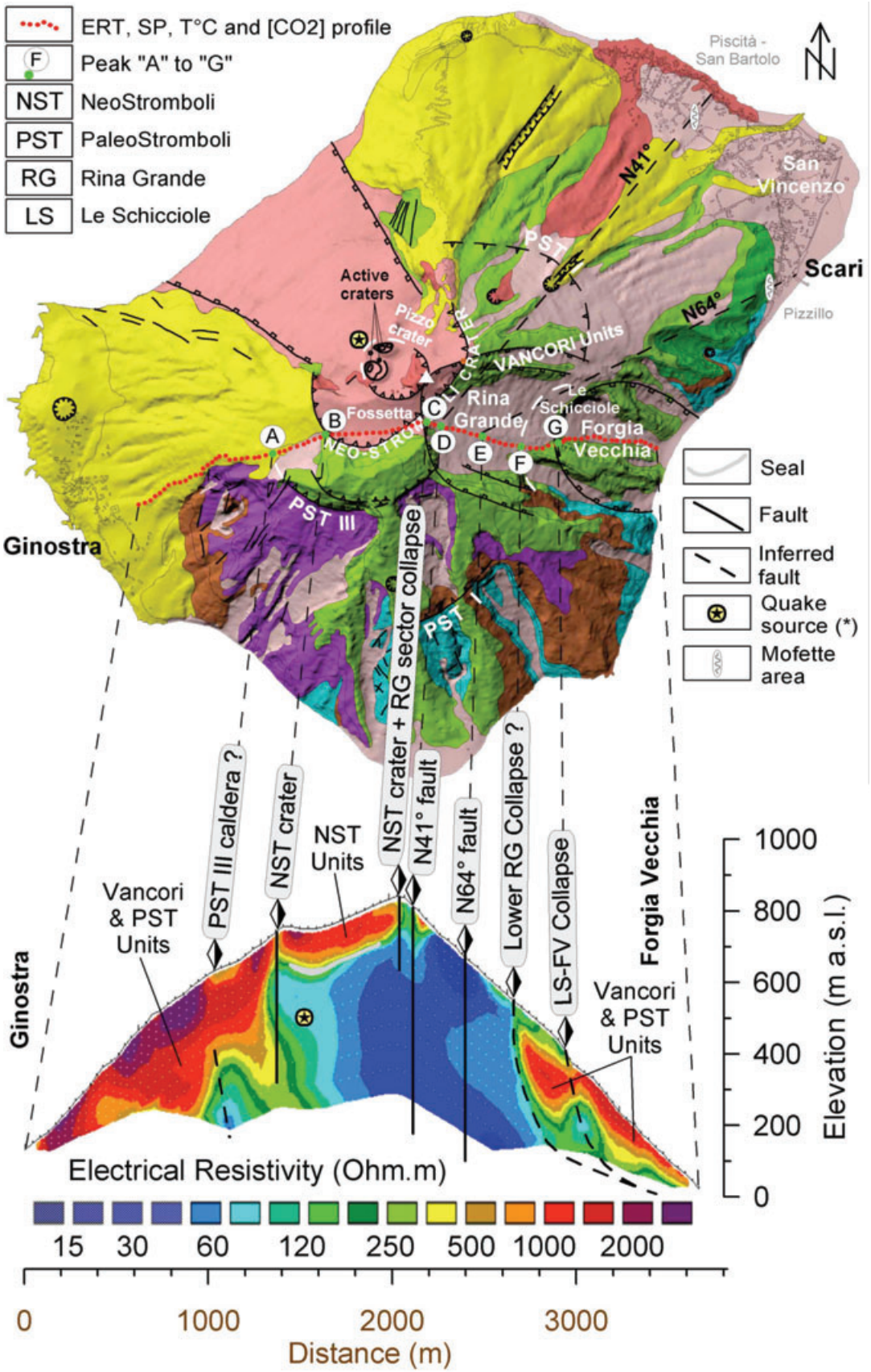

Figure 5. Interpreted DC resistivity tomogram (in ohm m) along Ginostra-Forgia Vecchia profile with the correlation of structural boundaries on the geological map. Vertical scaling factor for the resistivity inverted section from RES2DINV: 1.7. The filled star (⋆) represents the approximate source location of explosion quakes determined by Chouet *et al.* (2003). Other symbols: same as Fig. 2.

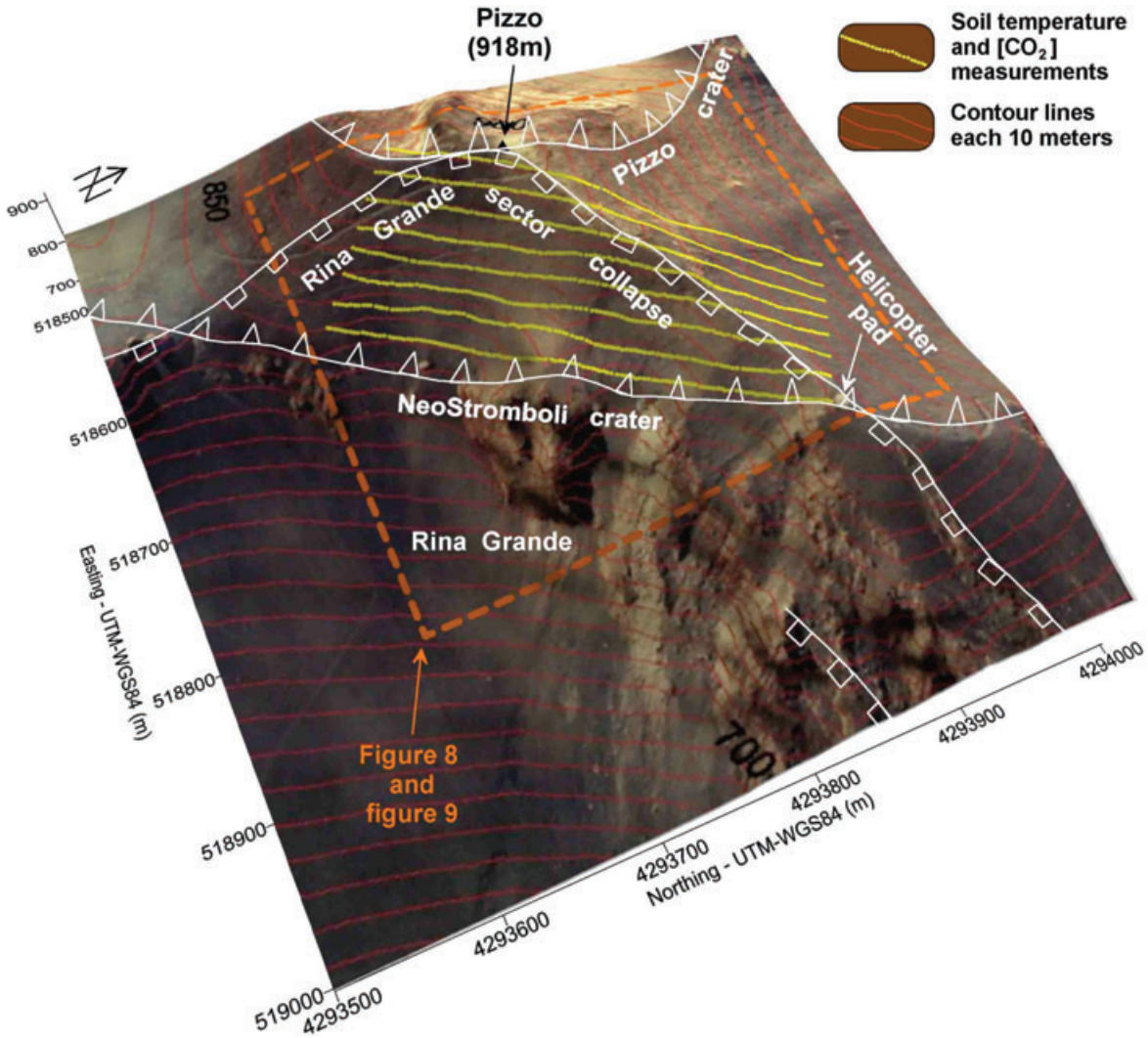

Figure 6. Position of the measurement stations for the survey of temperature, CO_2 soil concentration and self-potential measurements in the Pizzo area where some hydrothermal deposits are observed. The measurements are performed along eight profiles. The spacing between the measurement points along each profile is 2.5 m. The distance between the profiles is 20 m. Orthophoto and Digital Elevation Model (DEM) are courtesy of M. Marsella (Marsella *et al*. 2009).

usually associated with the upward flow of thermal fluids (Corwin & Hoover 1979; Richards *et al*. 2010) and possibly two-phase (liquid water and steam) flow (Byrdina *et al*. 2009).

A high-resolution survey (temperature, CO_2 concentration, CO_2 flux and self-potential measurements) of the Pizzo area is shown in Figs 6–9. Our data set shows that degassing and temperature anomalies are confined along a higher permeability pathway with an arched shape, localized between 'Pizzo' and 'helicopter pad', in the continuity of the northern structural boundary of the Rina Grande sector collapse (Figs 2, 6–9). Moreover, despite the fact that temperature measurements implies cold areas on both sides of the Rina Grande structural boundary (Fig. 8), the CO_2 degassing display a clear difference between both sides of this structural boundary. Carapezza *et al.* (2009) defined in this area five CO_2 flux populations based on probability plot technique (Sinclair 1974; see Fig. 9a). Inside the collapse structure of Rina Grande, the population corresponding to the lowest CO_2 flux (<6 g m^{-2} d) is located in the same area of the CO_2 concentration below atmospheric level (350 ppm, so below −1.5 in logarithmic scale, see dark blue colour area in Fig. 7). This means that some seals exist at depth. These seals may be influenced by the gliding plane of Rina Grande sector collapse. This importance of the Rina Grande sector collapse in driving hot hydrothermal fluids toward the summit part of the volcano is shown in the high-resolution survey (Figs 6–8). Note that the Ginostra-Scari profile does not cross the Rina Grande structural boundary but just brush against the head of this collapse structure. It is interesting to note that along the Ginostra-Scari profile, the maximum peak of CO_2 concentration (see position 'H' in Fig. 3) is not located on the Pizzo crater boundary but clearly 40 m in the East direction along the boundary of Rina Grande sector collapse (see position 'H' in Fig. 9). These characteristics regarding the location of the degassing anomalies imply that Rina Grande has a strong influence in both sealing and driving the magmatic and hydrothermal fluids toward the summit area (Pizzo area).

Considering the Ginostra-Scari profile, we interpret the central conductive body shown in Fig. 3 as the main hydrothermal system of the volcanic edifice. The low resistivity of the volcanic rocks can be due to the alteration of these materials (resulting in clay minerals and some zeolites with high surface conductivities, see Waxman & Smits 1968; Revil & Glover 1998; Revil & Leroy 2001), temperature, salinity, porosities or a combination of these factors (Revil 1999; Revil *et al*. 2002). A very good example of the interpretation

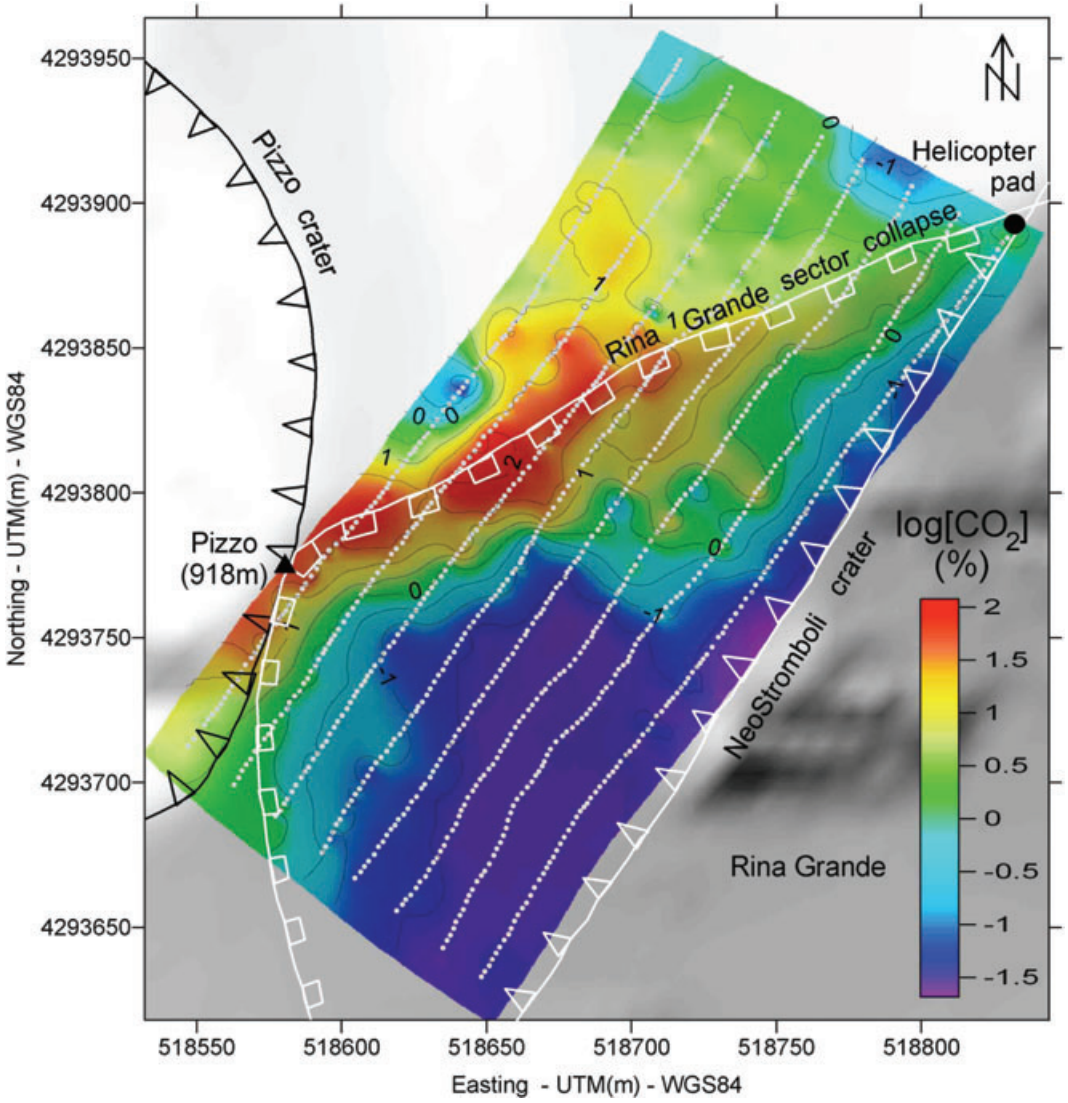

Figure 7. Soil CO_2 concentration map (logarithmic scale in per cent). Note that the highest concentrations are localized along the crest Pizzo to Helicopter pad, corresponding to the head of the gliding plane of the Rina Grande sector collapse. The value −1.5 per cent in logarithmic scale (equivalent to ∼350 ppm) corresponds to the atmospheric concentration of CO_2.

of resistivity measurements of a hydrothermal system is given by Komori *et al*. (2010) who were able to separate pore water and surface conductivity using downhole and core measurements. In the present case, we do not have access to such information. However, the use of a multidisciplinary approach as outlined above points out clearly that the conductive body is related to an important source of hot fluids rising and spreading along the major structural boundaries of the edifice. In some areas, like in the Fossetta area and in the upper part of the Rina Grande sector collapse area, the migration of the hydrothermal fluids are stopped by impermeable layers. We will discuss the origin of these layers below.

Along the Ginostra-Scari profile, the resistive body above the village of Ginostra (south west part of the edifice) is separated from the conductive hydrothermal system by the NeoStromboli crater fault ('B' in Figs 3 and 10). This resistive body corresponds to the Vancori and older (PaleoStromboli) Units, which consists of massive basaltic lava flows. It is not surprising that these units having very low-porosity (but heavily fractured in some areas) and not altered, have high resistivities (>1000 ohm m). The Vancori and PaleoStromboli Units are not associated with a self-potential anomaly (implying either no aquifer or a flat, still, aquifer located at a depth below the depth of exploration of our electrical resistivity tomography survey) and a normal soil CO_2 concentration accounting for the presence of vegetation (Fig. 3 and 10). For the case when an aquifer is present, the water may be channelled through fractures directly from the ground surface to this aquifer. In this area, a small CO_2 anomaly (anomaly 'A' in Figs 3 and 10) is associated with the axis of a deep conductive body, which is itself associated with a break in the topography. This CO_2 anomaly could represent the signature of a permeable pathway associated with a major structural boundary, namely the PaleoStromboli III caldera.

On the other side of the volcano (NE slope), we observe a shallow resistive body with a thickness of 50–120 m (Fig. 3). This resistive body is associated with the Vancori formation, which is heavily fractured on this side of the volcano. Four soil CO_2 concentration anomalies >10 000 ppm (these anomalies are denoted as 'H', 'I', 'J' and 'K' in Fig. 3), are possibly related to four major structural boundaries crossing the Vancori Unit. The 'H' anomaly is associated with the top of the Rina Grande sector collapse. The anomaly 'I' corresponds to the NeoStromboli crater. The anomaly 'J' is possibly

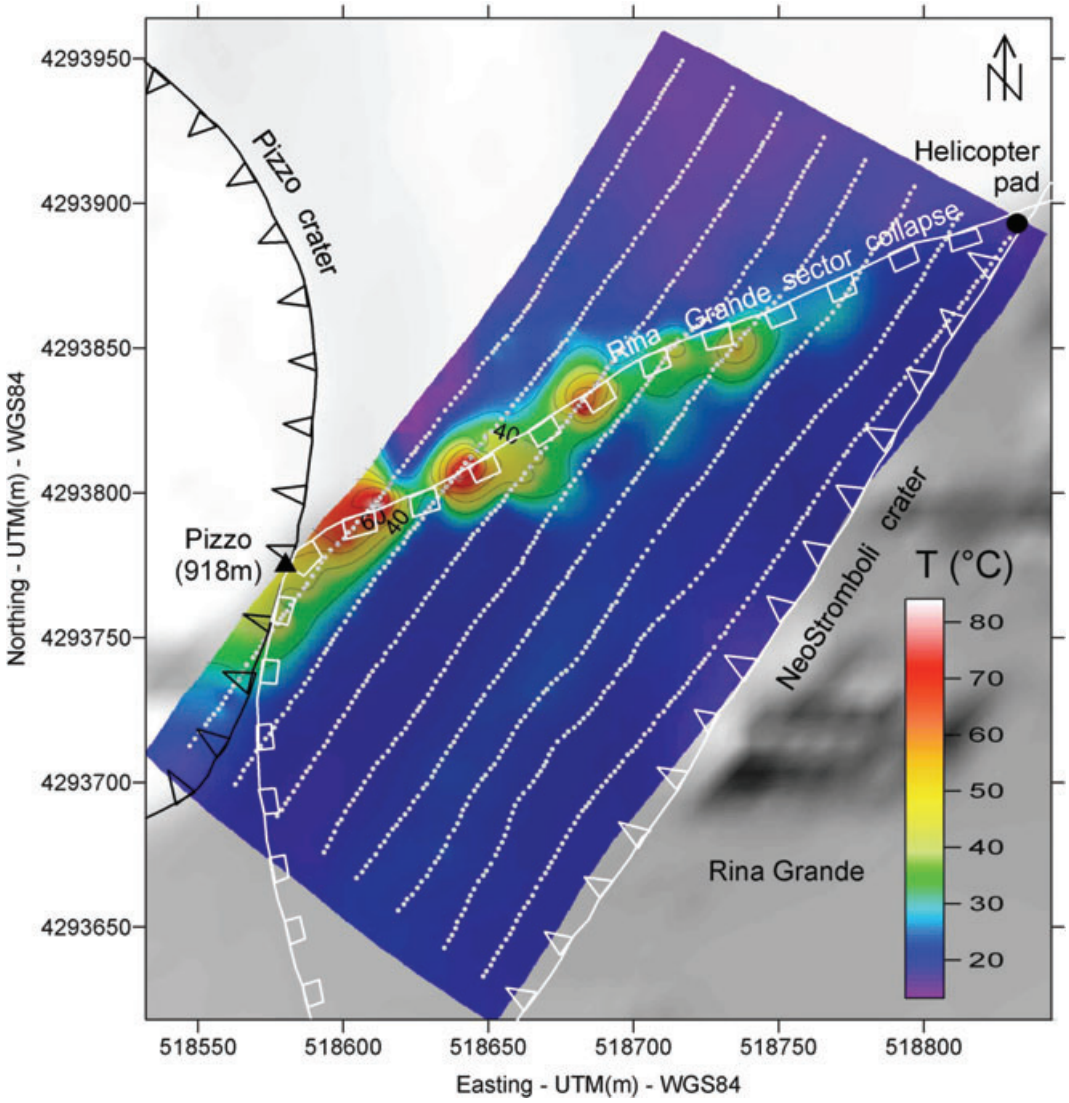

Figure 8. Temperature map at a depth of 30 cm. Note that the temperature anomaly is localized along the crest Pizzo to Helicopter pad, corresponding to the head of the gliding plane of the Rina Grande sector collapse.

associated with the continuity of the PaleoStromboli III Caldera. Finally, the anomaly 'K' corresponds to the regional N41° fault, associated itself with a small, but significant, increase in temperature (see Fig. 10). The conductive area observed in the central part of the edifice (see discussion above) seems to expand below the Vancori formation towards the sea. This may imply that the hydrothermal system extends to the sea on this side of the volcano. Such a mixing between hydrothermal fluids, fresh, and sea waters is shown in the area just above the village of Scari where the temperature of some wells reaches values between 40 and 44 °C. The self-potential signals show a negative trend with the elevation. This type of trend is classically related to the existence of an unconfined aquifer (e.g. Revil *et al*. 2004a; Richards *et al*. 2010 and references therein). On the NE lower flank of the edifice, the self-potential gradient versus elevation remains constant (–0.22 mV m^{-1}, see Fig. 3). This trend extends from a break in the self-potential data (see anomaly 'L') to the coast. This break in the slope 'L' is located on the structural boundary of the old PaleoStromboli I Caldera. This means that outside the PaleoStromboli I Caldera, an unconfined aquifer extends from about 400 m a.s.l. down to the sea with a lateral extend of about 2 km. An attempt to evaluate the depth of this aquifer is presented in Section 6.

A comparison between the electric resistivity tomography of Ginostra-Scari and the profile performed in 2004 (with a take-out every 20 m instead of 40 m, see Finizola *et al*. 2006) display numerous similarities including, for example, the deep influence on fluid flow of the SW boundary of the NeoStromboli Crater. There are also several intriguing differences both in electric resistivity tomography and in the self-potential and soil CO_2 concentration data: (1) For instance, the NE boundary of NeoStromboli crater, limiting the lateral extension of the hydrothermal system (see fig. 2 in Finizola *et al*. 2006), does not seem to play the same role in our survey (Fig. 6). (2) In the same sector (the upper NE flank of the edifice), the three peaks of CO_2 concentration, up to 10 000 ppm (see anomalies 'I', 'J' and 'K' in Fig. 4) do not have any equivalent in the profile performed in 2004 (see fig. 2 in Finizola *et al.* 2006). These differences can be easily explained due to the fact that the profile location between the Pizzo area and PaleoStromboli I caldera boundary is not the same in these two surveys. In 2004, the profile was located much closer to the northern Rina Grande

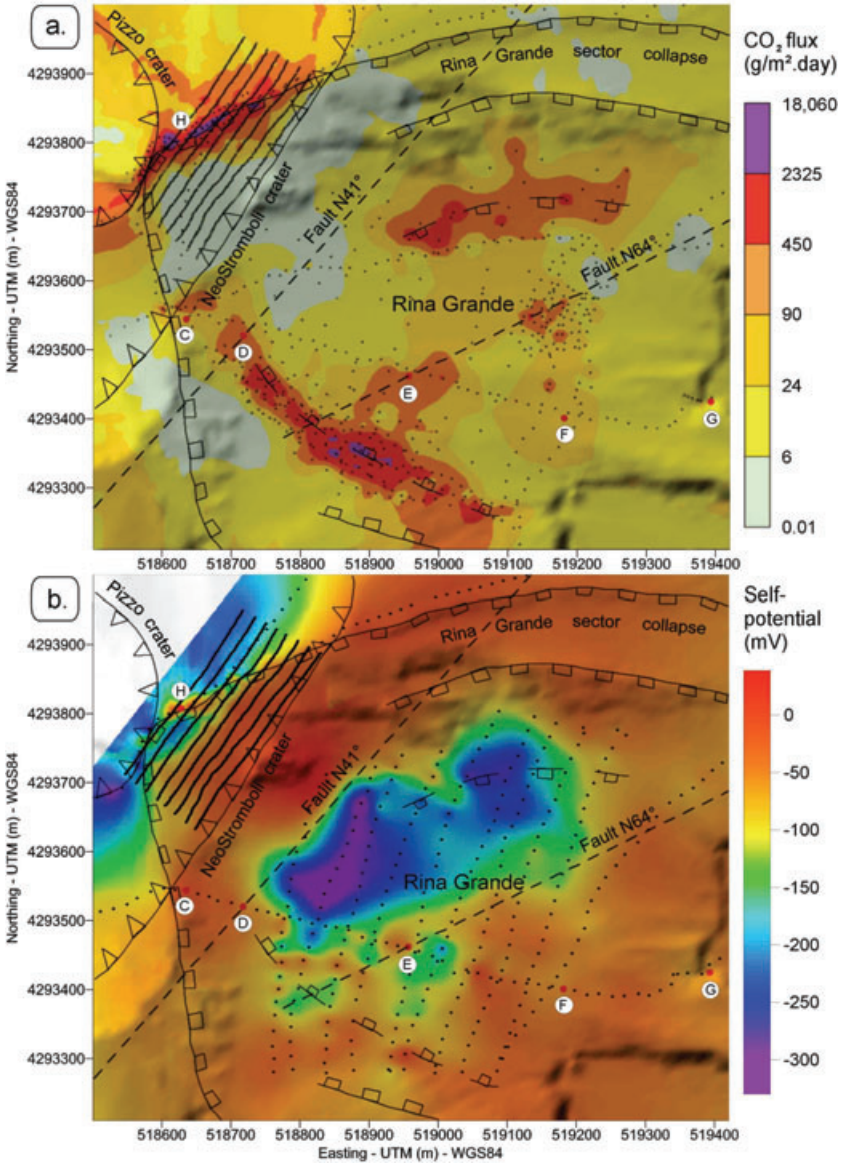

Figure 9. Comparison between the CO_2 flux map discussed in Carapezza *et al.* (2009) and the self-potential of the Rina Grande and Pizzo area (this work). The highest CO_2 flux values in the Rina Grande area are located along two curvilinear structures, in the northern and southern part of Rina Grande and correspond probably to a old gliding plane. A third high degassing area is located along the N64° fault (anomaly 'E' described in Fig. 4). A huge self-potential minimum (mauve colour) is located in the middle of Rina Grande between these three degassing structures and the faults N41° and N64°.

Sector collapse boundary than the profile carried out in 2011. It seems that, in the vicinity of the structural boundary of Rina Grande sector collapse, the influence of fracturation and faulting is smaller than several hundred meters in the north direction. This interesting result implies an inherent complexity in the organization of the geology of such stratovolcano edifices in term of permeability change along the same structural boundary at the scale of only several hundred meters.

5.2 Profile Ginostra-Forgia Vecchia and Rina Grande area

The resistivity tomogram of Profile Ginostra-Forgia Vecchia is shown in Fig. 4 with the self-potential, soil CO_2 concentrations and temperature measurements. Profile Ginostra-Forgia Vecchia is similar to the results of Profile Ginostra-Scari in the SW part of the edifice. Soil CO_2 concentration anomalies 'A' and 'B' may be associated with the PaleoStromboli III caldera and NeoStromboli crater faults, respectively (Fig. 5). This profile shows also that the hydrothermal system observed in the central part of the edifice extends towards the Eastern part of the volcanic edifice filling more than two-thirds of the Rina Grande area. Indeed a conductive body (resistivity <50 ohm m) can be clearly observed below the Rina Grande area where four strong soil CO_2 concentrations are observed (see anomalies 'C', 'D', 'E' and 'F' in Fig. 4). All these anomalies are associated with distinct structural boundaries with one exception. The anomaly 'C' is associated with the NeoStromboli crater boundary and the Rina Grande sector collapse. The anomaly 'D' is associated with the N41° regional fault. The anomaly 'E' corresponds to the N64° fault, which is also associated with CO_2 concentrations reaching values close to full saturation (Fig. 4). Finally, the anomaly 'F', which limits sharply the lateral extension of the hydrothermal system toward the East, is not associated to a known

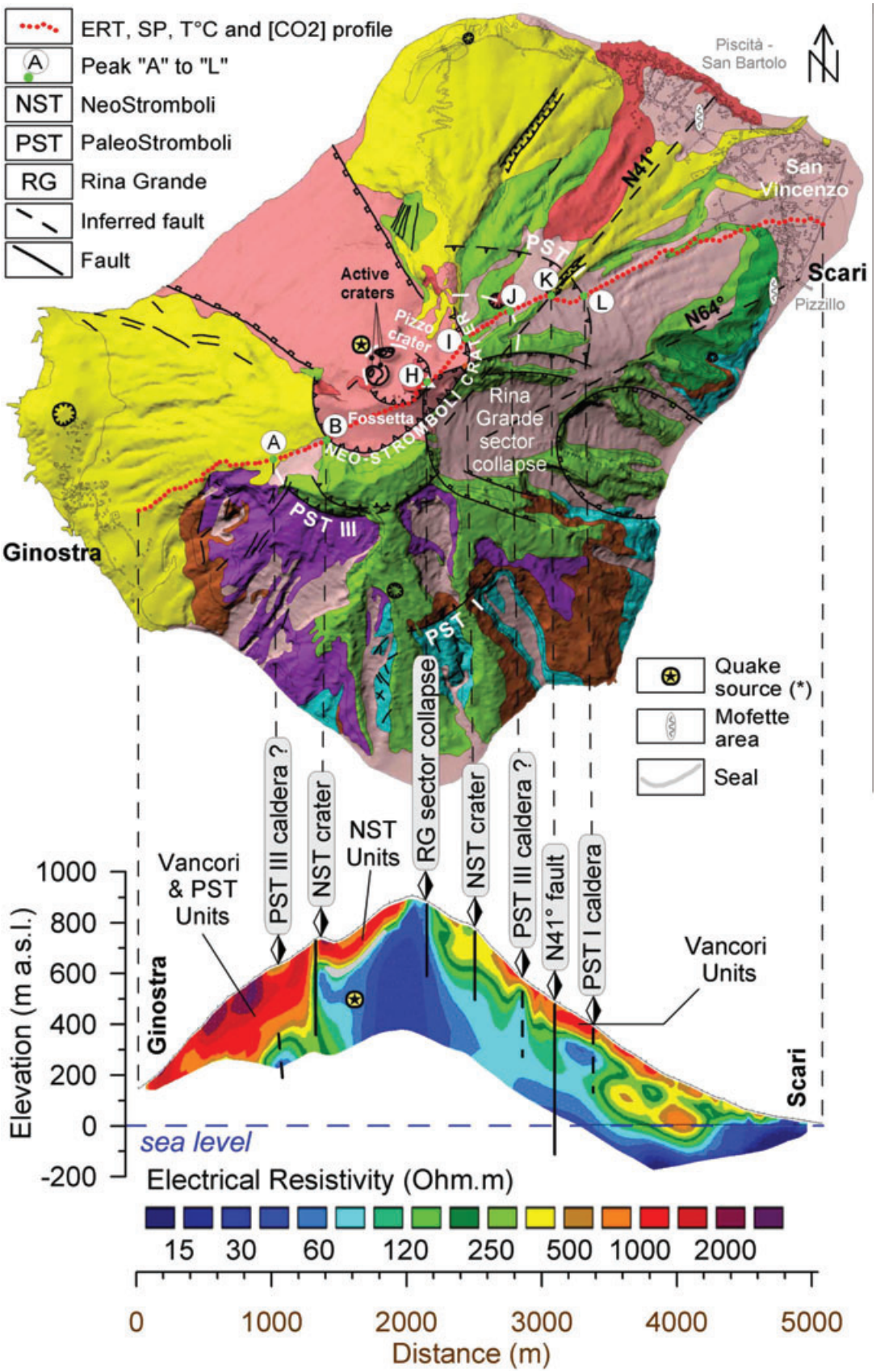

Figure 10. Interpreted DC resistivity tomogram (in ohm m) along Ginostra-Scari profile with the correlation of structural boundaries on the geological map. Vertical scaling factor for the resistivity inverted section from RES2DINV: 1.7. The filled star (⋆) represents the approximate source location of explosion quakes determined by Chouet *et al.* (2003). Other symbols: same as Fig. 2.

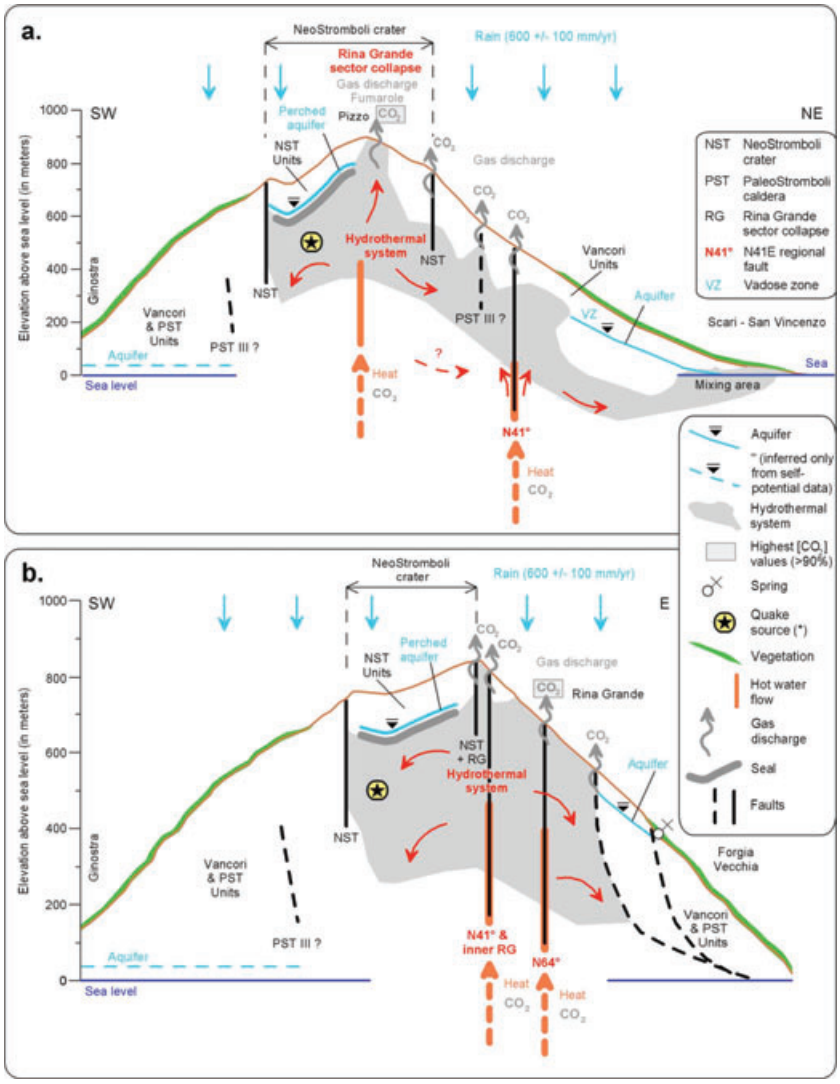

Figure 11. Interpretation of the two profiles in terms of fluid flow pathways. The low soil CO_2 concentration in the Fossetta implies the existence of a seal confining the hydrothermal system except at the positions of major faults of high permeability pathway for CO_2 rising systems: the fault bordering the Rina Grande sector collapse, the fault of the gliding plane limiting the lateral extension of the hydrothermal system toward the East in the lower part of Rina Grande area, and the regional fault N41° and N64°. (*) The filled-star represents the approximate source location of explosion quakes determined by Chouet *et al.* (2003). Note the relatively high rain rate of about 600 mm yr^{-1}.

structural boundary. Nevertheless, the electrical resistivity tomography (Fig. 5) strongly suggests that the boundaries 'F' and 'G' corresponds to two overlapped collapse structures oriented towards the east. The anomaly 'G' itself is associated with the 'Le Schicciole' collapse area (Pasquarè *et al*. 1993).

Maps of CO_2 flux measurements (Carapezza *et al.* 2009) and self-potential measurements (this work) are shown in Fig. 9. Inside the Rina Grande area, the CO_2 flux map displays three main degassing areas. Two of these areas, one on the north and one on the south, show a curvilinear orientation parallel to the already known inner collapse of Rina Grande. These areas are related to another smaller collapse structure overlapped inside the two other collapse structures of Rina Grande (see dashed lines in Fig. 9). The third degassing area is located between these two collapse boundaries and encompasses the positive 'E' anomaly of CO_2 concentration, temperature and self-potential (see anomaly 'E' in Figs 4 and 9). This anomaly is clearly elongated along a NE–SW axis corresponding to the N64° Fault. The self-potential map displays a strong negative self-potential anomaly in an area of approximately 200 m × 200 m (see the mauve colour in Fig. 9b). This negative anomaly is located between the three main degassing structures and a secondary minimum (see the blue colour in Fig. 9b) cutting the northern degassing structure. This self-potential minimum area is bordered by sharp self-potential gradients in agreement with the position of the N41° and N64° Faults. This area of negative self-potential anomaly could be interpreted as the result of downward water infiltration dragged along the shallowest collapse(s) gliding plane(s) of the Rina Grande area. According to this hypothesis, the N41° fault could have played a role in the historical collapse of Rina Grande.

6 DISCUSSION OF THE GENERAL FLOW PATTERN

The general flow pattern for the two profiles is summarized in Fig. 11. According to Aizawa *et al*. (2005) (see also Fitterman *et al*.

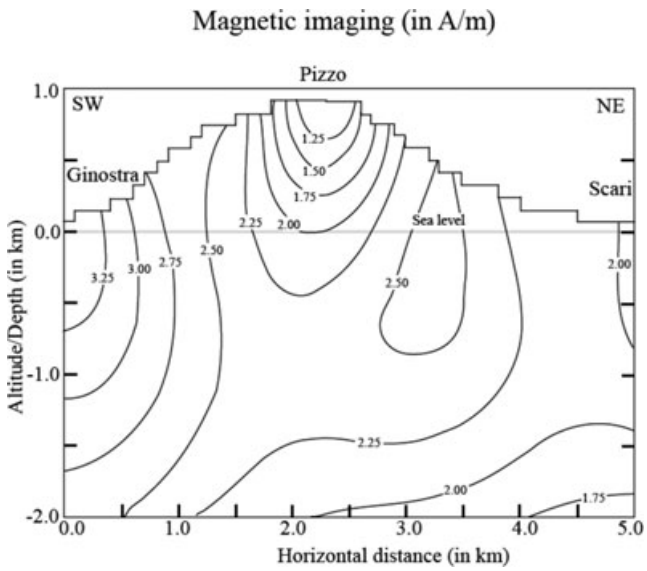

Figure 12. Cross-section of 3-D magnetic imaging of Stromboli volcano and its vicinity (modified from Okuma *et al*. 2009). Contour interval is 0.25 A m^{-1}. Vertical exaggeration is 1.25. The area with low magnetization (<2.50 A m^{-1}) corresponds to the hydrothermal system (Figs 3 and 11a) while areas with high magnetization (>2.50 A m^{-1}) correspond to less altered lava flows.

1988), the conductive zone in a volcanic edifice is considered to correspond to the zone of coexisting clay (resulting from alteration) and hot fluids with temperatures below 200 °C, both associated with the hydrothermal system. Following this idea, the conductive body observed in the central part of the edifice is interpreted as the main hydrothermal system. This interpretation is consistent with the volume of low magnetization observed by Okuma *et al*. (2009) in the central part of Stromboli (Fig. 12).

The range of resistivity values for the hydrothermal system (15–50 ohm m) is consistent with the resistivity considered by Aizawa *et al*. (2005) for Japanese stratovolcanoes. The heat and CO_2 degassing source are associated with the existence of a shallow storage of magma below the active vents. Indeed, Chouet *et al*. (2003) showed that the source of explosion quakes and tremor are associated with the summit part of the shallower feeding system and are located at depths of approximately 220 m beneath and 160 m northwest of the active vents (see the position of the star in Fig. 11).

On the Western side of the edifice, the hydrothermal system is confined by the fault bordering the NeoStromboli crater. The evidence of atmospheric levels of soil CO_2 concentrations (360 ppm) in the Fossetta implies the existence of a seal capping the hydrothermal system. Similar conclusions have been reached by Aizawa *et al*. (2009, their fig. 5) for some Japanese stratovolcanoes. According to Finizola *et al.* (2002), Revil *et al*. (2004b) and Aizawa *et al*. (2009), the upper layer of the hydrothermal system is largely sealed by clay-rich materials. A striking example of such a seal is discussed by Revil *et al*. (2004b) for the summit crater of Stromboli. The permeability of these seals is so low that CO_2 is prevented to cross such a boundary. The occurrence of seals in hydrothermal systems is common (e.g., Facca & Tonani 1967; Ingebritsen & Sorey 1988; Lowell *et al*. 1993 and references therein). The infiltration of meteoric water can flow on the upper side of such a seal to form a perched aquifer (Fig. 11, Finizola *et al.* 2002 and Revil *et al*. 2004b, for an example).

The sealing of hydrothermal systems is also supported by the fact that surface geothermal activity and gas discharge is generally highly localized where faults are located (see the examples given by Finizola *et al.* 2002, 2006; Revil *et al*. 2004b). In our case, only the fault bordering the head of the Rina Grande sector collapse near the Pizzo area exhibits a strong near surface (30 cm deep) temperature anomaly (>80 °C, see Figs 3 and 8). High soil CO_2 concentrations are usually indicative of the presence of open faults, fractures and limits of collapse zones.

The adventive hydrothermal circulation on the NE side of the volcanic cone is consistent with the observations of Finizola *et al.* (2010) and wells at Scari and San Vincenzo recording a ground water temperature of about 40 °C. Regarding the downward extension of the hydrothermal system, we can use the preliminary inversion of aeromagnetic data by Okuma *et al.* (2009) (Fig. 12). The profile shown in Fig. 12 is characterized by the lowest magnetization in the central part of the edifice corresponding to the hydrothermal system and higher magnetization along the flanks corresponding to lava flows. This implies a much deeper root for the main hydrothermal system.

Adventive hydrothermal circulation seems also to exist below the Rina Grande area. Because of the mechanical weakening of the rocks by long-standing thermal alteration, such an observation may explain the various collapses observed in this area (Figs 2 and 9). This alteration could represent a risk of future collapses. This area should be therefore better imaged in 3-D and monitored continuously in terms of deformation.

Finally, we investigate the possible position of the aquifer above the villages of Scari and San Vincenzo by interpreting semi-quantitatively the self-potential in the NE part of the volcano (end part of Profile Ginostra-Scari). We first need to determine a reasonable value for the streaming potential coupling coefficient, which represents the sensitivity between the electrical potential difference produced in response to a pore fluid pressure gradient. We measure this coupling coefficient for a set of seven samples taken from the Rina Grande area because this area is likely to represent an outcrop of the section above Scari along which we expect to find the aquifer. These samples were first crushed, washed to remove organic matter, and sieved to obtain a grain size comprises between 100 and 200 μm. The samples were saturated with NaCl electrolytes at different ionic strengths during several days. In order to be certain that equilibrium is reached, the conductivity and the pH of the solution were measured over time. The methodology used to perform these measurements is described in Revil *et al*. (2004b) with two non-polarizing Ag/AgCl electrodes located at the end faces of the sample. The sample is enclosed in a glass holder allowing fluid flow only through the two end faces. We measure the electrical potential difference between the two end-faces of the sample submitted to a known pore fluid pressure difference in drained conditions. The results (Fig. 13) show that the coupling coefficient depends strongly on the conductivity of the pore water as predicted by the electrokinetic theory. The ground water at Le Schicciole seasonal spring, which is located in between the Rina Grande and Le Schicciole areas, was sampled. Its electrical conductivity is 0.128 ± 0.001 S m^{-1} (at 25 °C). Interestingly, Revil *et al*. (2004b) placed demineralized pore water in contact with volcanic ashes collected inside the Pizzo crater area. The electrical conductivity was monitored over several days indicating that it reached equilibrium in less than 2 d. They obtained a water conductivity value in equilibrium with the volcanic ash of 0.1 S m^{-1} (at 25 °C) in agreement with the previous value.

The streaming potential coupling coefficient is between -0.6 mV m^{-1} and -2.5 ± 1.0 mV m^{-1} with a likely value of -1.2 mV m^{-1}. If the self-potential trend observed in the NE part of the volcano is related to the presence of an unconfined aquifer,

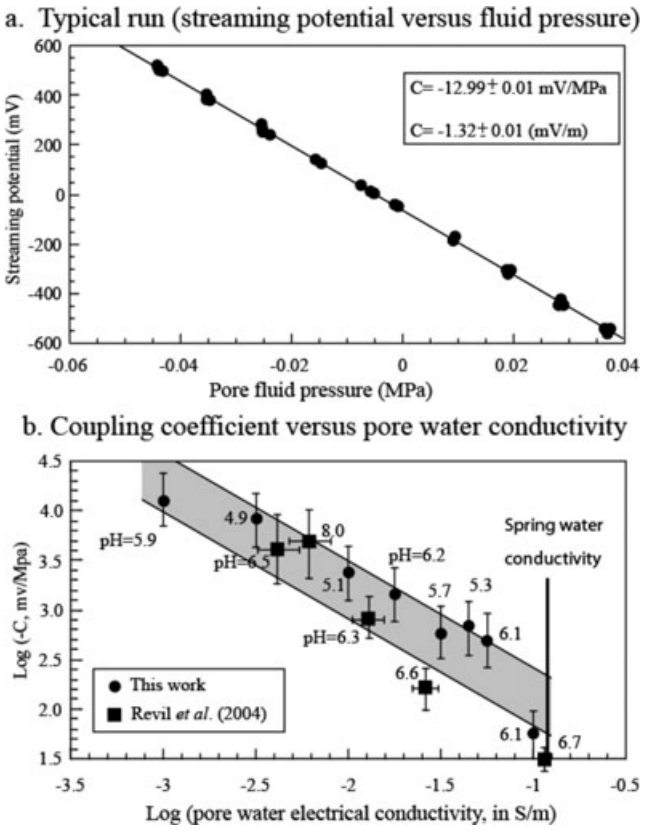

Figure 13. Measurements of the streaming potential coupling coefficient. (a). Laboratory measurements of the streaming potential coupling coefficient. The streaming potential coupling coefficient is given as a slope of the recorded electric potential versus the fluid pressure differentials imposed between the two end-faces of a cylindrical core sample. (b) Measured streaming potential coupling coefficient C versus the fluid conductivity. The pH values represent the pH of solution in equilibrium with the core sample and the atmosphere. The spring water conductivity has been measured at the (seasonal) spring of Le Schicciole. Comparison with the data from Revil *et al.* (2004b) using scoria from Stromboli. The grey area corresponds to the expected linear trend in a log–log plot.

we can roughly estimate the elevation of the water table as follow. We consider the reference at the sea level (0 mV). At the boundary of the aquifer defined with a constant self-potential/elevation ratio (see anomaly 'L' in Fig. 3), the self-potential signal is −110 mV in the case of profile Ginostra-Scari. There are several models that link self-potential signals to the depth (or the elevation) of the water table (see Jackson & Kauahikaua 1987; Aubert & Atangana 1996 for early investigations and Aizawa *et al*. 2009; Onizawa *et al*. 2009; Ball *et al*. 2010, for more recent studies). Taking the above value for the streaming potential coupling coefficient and assuming that the self-potential response is controlled by the hydraulic head yields a hydraulic head of 100 ± 60 m at the hydrothermal/aquifer contact. This estimate and the fact that the elevation of the aquifer is null at the shore line are used to sketch the position of the aquifer in Fig. 11.

Keeping a distance of about 1.5 km between the sea shore and the boundary between the aquifer and the hydrothermal system (corresponding to the position 'L' in fig. 3), this yields a hydraulic head gradient of 0.05 for the unconfined aquifer. According to the Ghyben-Herzberg formula (based on isostatic equilibrium, see Domenico & Schwartz 1990; Michael *et al*. 2005) in an homogeneous island, the interface between the fresh water and the sea water occurs at a depth below sea level that is 40 times the height of the water table (above sea level). The depth of the sea water intrusion could be as low as 3 km b.s.l. below the boundary between this aquifer and the hydrothermal system, so very deep inside the volcano. We plan to check this assumption by using MT measurements in a future work.

On the SW part of the island, the −50 mV anomaly could imply a relatively flat aquifer with a water table elevation of 40 m a.s.l. assuming that the streaming coupling coefficient is equal to -1.2 mV m^{-1}. This assumption is usually valid as long as the effect of surface conductivity associated with clays and zeolites is negligible (Revil *et al*. 2003, their fig. 3). In turn, this would imply a depth of the sea water intrusion deeper than 1.5 km according to the Ghyben-Herzberg relationship.

7 CONCLUDING STATEMENTS

This study allowed us to constrain the hydrogeology of the Stromboli volcanic island in the Aeolian Archipelago in Italy. The following conclusions have been reached:

1. A hydrothermal system (resistivity in the range 15–50 ohm m) is located in the central part of the volcanic edifice and extending in both the NE and E directions. In the NE direction it explains why warm water is found at the villages of Scari and San Vincenzo (temperature in the range 40–44 °C). In the Rina Grande collapse area (E direction), the existence of the hydrothermal system explains the high degassing rate of this zone also crossed by two major faults (N41° and N64°). The existence of a hydrothermal body is consistent with low magnetizations ($<$2.5 A m^{-1}) in these areas. Our survey points out that the Rina Grande sector collapse is one of the most important structural control for magmatic and hydrothermal fluids in the upper part of Stromboli volcanic edfice. This area, formed of three horse shoe-shape overlapping structures opened toward the east, is responsible of the two main diffuse degassing areas in the upper part of the edifice. (a) The first degassing area is associated with the top of the largest horse shoe-shape structure dragging magmatic fluids toward the summit area (more precisely toward the Pizzo area; see anomaly 'H' in both Figs 3 and 9). The second degassing area is associated with the smallest horse shoe-shape structure, which drags also hydrothermal and magmatic fluids along its southern border. In addition, the Rina Grande sector collapse is characterized by the shallow depth of the hydrothermal system of Stromboli. In the lower Eastern part of the Rina Grande area, the lateral extension of the hydrothermal system is constrained by another boundary of sector collapse, located less than 200 m in distance above the Le Schicciole sector collapse delimitating the Forgia Vecchia area.

2. There is no evidence for a shallow hydrothermal system in the SW part of the edifice above the village of Ginostra. The resistivity models show a resistive body (in the range 1000–3000 ohm m) that could be associated with the Vancori and PaleoStromboli units. This assumption is confirmed with a higher magnetization of this area ($>$2.5 A m^{-1}).

3. The self-potential data show the presence of an unconfined aquifer above the village of Scari. A simple order of magnitude estimate from the self-potential data leads to a slope of 0.05 for this aquifer (50 m of head per kilometre).

The information discussed above should be combined with additional information (especially magnetic and gravity) to perform a 3-D joint inversion of these geophysical data. The use of the resistivity information would allow reducing the non-uniqueness of

the inverse problem in inverting the magnetic data alone. 3-D resistivity tomography of Vulcano has been performed recently by Revil *et al.* (2010). Such type of work could be performed at Stromboli as well. Numerical models simulating volcanic hydrothermal systems (see Ingebritsen *et al*. 2010) require accurate and detailed geophysical investigations. We envision that our study can be the basis for such a work integrating geological, geophysical, and hydrogeological information in an accurate numerical investigation of the hydrothermal system of Stromboli. Such modelling could be useful to monitor this volcano.

ACKNOWLEDGMENTS

The INSU-CNRS, the Laboratoire GéoSciences Réunion-IPGP, the Istituto Nazionale di Geofisica e Vulcanologia (INGV) and the DOE (Energy Efficiency and Renewable Energy, Geothermal Technologies Program, award DE-FG36–08GO018195) are thanked for funding. We thank the personnel of the National Civil Protection and Mario Zaia (Zazà) for their continuous support during the field survey. This is the IPGP contribution number 3148. We thank Jean-François Lénat for the use of the resistivity equipment (co-funded by the Laboratoire GéoSciences Réunion of Reunion Island, the Laboratoire Magmas et Volcans of Clermont-Ferrand, and the INSU-CNRS), Gladys Le Masson, Casi Lock, Xavier Rassion, Barbara Suski, Agnès Crespy and Nicole Wolyniec for their help during the 2011 January field campaign for the two geoelectrical profiles crossing the island. Emilie Roulleau and Julie Morin are also thanks for their help in 2006 May for the fieldwork performed in the summit area of Pizzo. AF thanks Laurent Michon for fruitful discussions. We thank the Editor, Joachim Wassermann, Theodore H. Asch and one anonymous referee for the constructive reviews of our manuscript.

REFERENCES

Aizawa, K. *et al*. 2005. Hydrothermal system beneath Mt. Fuji volcano inferred from magnetotellurics and electric self-potential, *Earth planet. Sci. Lett.*, **235**, 343–355, doi:10.1016/j.epsl.2005.03.023.

Aizawa, K., Ogawa, Y. & Ishido, T., 2009. Groundwater flow and hydrothermal systems within volcanic edifices: delineation by electric self-potential and magnetotellurics, *J. geophys. Res.*, **114**, B01208, doi:10.1029/2008JB005910.

Apuani T., Corazzato C., Cancelli A. & Tibaldi A., 2005. Stability of a collapsing volcano (Stromboli, Italy): limit equilibrium analysis and numerical modeling, *J. Volc. Geotherm. Res.*, **144**, 191–210, doi:10.1016/j.jvolgeores.2004.11.028.

Aubert, M. & Yene Atangana, Q., 1996. Self-potential method in hydrogeological exploration of volcanic areas, *Ground Water*, **34**(6), 1010–1016.

Ball L., Ge, S., Caine, J.S., Revil, A. & Jardani, A., 2010. Constraining fault-zone hydrogeology through integrated hydrological and geoelectrical analysis, *Hydrogeol. J.*, 1057–1067, **18**, doi:10.1007/s10040–010-0587-z.

Barberi, F., Civetta, L., Gasparini, P., Innocenti, F., Scandone, R. & Villari, L., 1974. Evolution of a section of the Africa-Europe plate boundary; paleomagnetic and volcanological evidence from Sicily, *Earth planet. Sci. Lett.*, **22**(2), 123–132.

Barberi, F., Bertagnini, A., Landi, P. & Principe, C., 1992. A review on phreatic eruptions and their precursors, *J. Volc. Geotherm. Res.*, **52**, 231–246, doi:10.1016/0377–0273(92)90046-G.

Barberi, F., Rosi, M. & Sodi, A., 1993. Volcanic hazard assessment at Stromboli based on review of historical data, *Acta Vulcanol.*, **3**, 173–187.

Bonaccorso, A., Calvari, S., Garfì, G., Lodato, L. & Patanè, D., 2003. Dynamics of the December 2002 flank failure and tsunami at Stromboli volcano inferred by volcanological and geophysical observations, *Geophys. Res. Lett.*, **30**(18), 1941, doi:10.1029/2003GL017702.

Byrdina, S. *et al*. 2009. Dipolar self-potential anomaly associated with carbon dioxide and radon flux at Syabru-Bensi hot springs in central Nepal, *J. geophys. Res.*, **114**, B10101, doi:10.1029/2008JB006154.

Carapezza, M.L. & Federico C., 2000. The contribution of fluid geochemistry to the volcano monitoring of Stromboli, *J. Volc. Geotherm. Res.*, **95**, 227–245.

Carapezza, M.L., Ricci, T., Ranaldi, M. & Tarchini, L., 2009. Active degassing structures of Stromboli and variations in diffuse CO_2 output related to the volcanic activity, *J. Volc. Geotherm. Res.*, **182**, 231–245.

Cardiff, M., Barrash, W., Kitanidis, P.K., Malama, B., Revil, A., Straface, S. & Rizzo, E., 2009. A potential-based inversion of unconfined steady-state hydraulic tomography, *Ground Water*, **47**(2), 259–270.

Carrera, J., Alcolea, A., Medina, A., Hidalgo, J. & Slooten, L.J., 2005. Inverse problem in hydrogeology, *Hydrogeol. J.*, **13**(1),206–222.

Chouet, B. *et al*., 2003. Source mechanisms of explosions at Stromboli Volcano, Italy, determined from moment–tensor inversions of very-long-period data. *J. geophys. Res.*, **108**(B1), 2019. doi:10.1029/2002JB001919.

Coppo, N. *et al*., 2008. Multiple caldera collapses inferred from the shallow electrical resistivity signature of the Las Canadas caldera, Tenerife, Canary Islands, *J. Volc. Geotherm. Res*, **170**(3–4), 153–166.

Corwin, R.F. & Hoover, D.B., 1979. The Self-Potential method in geothermal exploration, *Geophysics*, **44**, 226–245.

Cruz, J.V. & França, Z., 2006. Hydrogeochemistry of thermal and mineral water springs of the Azores archipelago (Portugal), *J. Volc. Geoth. Res.*, **151** (4), 382–398.

Domenico, P.A. & Schwartz, F.W., 1990. *Physical and Chemical Hydrogeology*, 2nd edn, John Wiley and Sons, New York, NY, 824pp.

Etiope, G., Beneduce, P., Calcara, M., Favali, P., Frugoni, F., Schiattarella, M. & Smriglio, G., 1999. Structural pattern and CO_2-CH_4 degassing of Ustica island, Southern Tyrrhenian basin, *J. Volc. Geotherm. Res.*, **88**, 291–304.

Facca, G. & Tonani F., 1967. The self-sealing geothermal field, *Bull. Volcanol.*, **30**, 271–273, doi:10.1007/BF02597674.

Finizola, A., Sortino, S., Lénat, J.-F. & Valenza, M., 2002. Fluid circulation at Stromboli volcano (Aeolian Islands, Italy) from self-potential and CO_2 surveys, *J. Volc. Geotherm. Res.*, **116**, 1–18.

Finizola, A., Sortino, S., Lénat, J.-F., Aubert, M., Ripepe, M. & Valenza, M., 2003. The summit hydrothermal system of Stromboli. New insights from self-potential, temperature, CO_2 and fumarolic fluid measurements. Structural and monitoring implications, *Bull. Volcanol.*, **65**, 486–504.

Finizola, A. *et al*., 2006. Hydrogeological insights at Stromboli volcano (Italy) from geoelectrical, temperature, and CO_2 soil degassing investigations, *Geophys. Res. Lett.*, **33**, L17304, doi:10.1029/2006GL026842.

Finizola, A. *et al.*, 2010. Adventive hydrothermal circulation on Stromboli volcano (Aeolian Islands, Italy) revealed by geophysical and geochemical approaches: Implications for general fluid flow models on volcanoes, *J. Volc. Geotherm. Res.*, **196**, 111–119.

Fitterman, D.V., Stanley W.D. & Bisdorf, R.J., 1988. Electrical structure of Newberry volcano, Oregon, *J. geophys. Res.*, **93**, 10 119–10 134.

Francalanci, L., 1987. Evoluzione vulcanologica e magmatologica dell'isola di Stromboli (Isole Eolie) : Relazioni tra magmatismo calc-alcalino e shoshonitico, Tesi di Dottorato, *PhD thesis*. Dipartimento di Scienze della Terra, Firenze.

Gélis, C., Revil, A., Cushing, M.E., Jougnot, D., Lemeille, F., Cabrera, J., De Hoyos, A. & Rocher, M., 2010. Potential of electrical resistivity tomography to detect fault zones in limestone and argillaceous formations in the experimental site of Tournemire, France, *Pure appl. Geophys.*, **167**(11), 1405–1418, doi:10.1007/s00024–010-0097-x.

Gillot, P.Y., 1984. Datation par la méthode du potassium argon des roches volcaniques récentes (pléistocènes et holocènes). Contribution à l'étude chronostratigraphique et magmatologique des provinces volcaniques de Campanie, des îles éoliennes, de Pantelleria (Italie du Sud) et de la Réunion (Océan Indien), *PhD thesis,* Paris.

Gillot, P.Y. & Keller, J., 1993. Radiochronological dating of Stromboli, *Acta Vulcanol.*, **3**, 69–77.

Hornig-Kjarsgaard, I., Keller, J., Koberski, U., Stadlbauer, E., Francalanci, L. & Lenhart, R., 1993. Geology, stratigraphy and volcanological evolution of the island of Stromboli, Aeolian arc, Italy., *Acta Vulcanol.*, **3**, 21–68.

Ingebritsen, S. E. & Sorey, M. L., 1988. Vapor-dominated zones within hydrothermal systems: Evolution and natural state, *J. geophys. Res.*, **93**, 13,635– 13,655, doi:10.1029/JB093iB11p13635.

Ingebritsen, S. E., Geiger, S., Hurwitz, S. & Driesner, T., 2010. Numerical simulation of magmatic hydrothermal systems, *Rev. Geophys.*, **48**, RG1002, doi:10.1029/2009RG000287.

Jackson, D.B. & Kauahikaua, J., 1987. Regional SP anomalies at Kilauea, *Volcanism in Hawaii*. USGS Prof. paper 1350, ch. 40, pp. 947–959.

Keller, J., Hornig-Kjarsgaard, I., Koberski, U., Stadlbauer, E. & Lenhart, R., 1993. Geological map of the island of Stromboli, *Acta Vulcanol.*, **3**.

Krivochieva, S. & Chouteau, M., 2003. Integrating TDEM and MT methods for characterizing and delineation of the Santa Catarina aquifer (Chalco Sub-basin, Mexico), *J. appl. Geophys.*, **52**(1), 23–43.

Komori, K., Kagiyama, T., Hoshizumi H, Takakura, S. & Mimura, M., 2010. Vertical mapping of hydrothermal fluids and alteration from bulk conductivity: simple interpretation on the USDP-1 site, Unzen Volcano, SW Japan, *J. Volc. Geotherm. Res.*, **198**, 339–347.

Loke, M.H., & Barker, R.D., 1996. Practical techniques for 3D resistivity surveys and data inversion, *Geophys. Prospect.*, **44**, pp. 499–523.

López, D. L. & Williams, S. N., 1993. Catastrophic volcanic collapse: Relation to hydrothermal processes, *Science*, **260**, 1794–1796, doi:10.1126/science.260.5115.1794.

Lorenz, V. & Kurszlaukis, S., 2007. Root zone processes in the phreatomagmatic pipe emplacement model and consequences for the evolution of maar-diatreme volcanoes, *J. Volc. Geotherm. Res.*, **159**(1–3), 4–32.

Lowell, R.P., Cappellen, P.V. & Germanovich, L.N., 1993. Silica precipitation in fractures and the evolution of permeability in hydrothermal upflow zones, *Science*, **260**, 192–194, doi:10.1126/science.260.5105.192.

Marsella, M., Proietti, C., Sonnessa, A., Coltelli, M., Tommasi, P. & Bernardo, E., 2009. The evolution of the Sciara del Fuoco subaerial slope during the 2007 Stromboli eruption: relation between deformation processes and effusive activity. *J. Volc. Geotherm. Res*, doi:10.1016/j.jvolgeores.2009.02.002.

Michael H.A., Mulligan A.E., & Harvey C.F., 2005. Seasonal oscillations in water exchange between aquifers and the coastal ocean, *Nature*, **436**, 1145–1148, doi:10.1038/nature03935.

Nappi, G., Capaccioni B., Biagiotti F., & Vaselli O., 1999. Upper pyroclastic sequence of the Scari formation: A paroxistic eruption from Stromboli volcano (Aeolian Island, Italy), *Acta Vulcanol.*, **11**, 259–264.

Okuma, S., Stotter, C., Supper, R., Nakatsuka, T., Furukawa, R. & Motschka, K., 2009. Aeromagnetic constraints on the subsurface structure of Stromboli Volcano, Aeolian Islands, Italy, *Tectonophysics*, **478**, 19–33.

Onizawa, S., Matsushima, N., Ishido, T., Hase, H., Takakura, S. & Nishi, Y., 2009. Self-potential distribution on active volcano controlled by three-dimensional resistivity structure in Izu-Oshima, Japan, *Geophys. J. Int.*, **178**, 1164–1181, doi:10.1111/j.1365–246X.2009.04203.x

Pasquarè, G., Francalanci, L., Garduno, V.H. & Tibaldi, A., 1993. Structure and geologic evolution of the Stromboli volcano, Aeolian Islands, Italy, *Acta Vulcanol.*, **3**, 79–89.

Petrinovic, I.A. & Piñol, F.C., 2006. Phreatomagmatic and phreatic eruptions in locally extensive settings of Southern Central Andes: the Tocomar Colcanic Center (24°10′S–66°34′W), Argentina, *J. Volc. Geotherm. Res.*, **158**(1–2), 37–50.

Revil A., 1999. Ionic diffusivity, electrical conductivity, membrane and thermoelectric potentials in colloids and granular porous media: a unified model, *J. Coll. Interface Sci.*, **212**, 503–522.

Revil, A. & Glover, P.W.J., 1998. Nature of surface electrical conductivity in natural sands, sandstones, and clays, *Geophys. Res. Lett.*, **25**(5), 691–694.

Revil, A. & Leroy, P., 2001. Hydroelectric coupling in a clayey material, *Geophys. Res. Lett.*, **28**(8), 1643–1646.

Revil, A., Hermitte, D., Spangenberg, E. & Cochémé, J.J., 2002. Electrical properties of zeolitized volcaniclastic materials, *J. geophys. Res.*, **107**(B8), 2168, doi: 10.1029/2001JB000599.

Revil, A., Naudet, V., Nouzaret, J., & Pessel, M., 2003. Principles of electrography applied to self-potential electrokinetic sources and hydrogeological applications, *Water Resour. Res.*, **39**(5), 1114, doi: 10.1029/2001WR000916.

Revil, A., Naudet, V. & Meunier J. D., 2004a. The hydroelectric problem of porous rocks: Inversion of the water table from self-potential data, *Geophys. J. Int.*, **159**, 435–444.

Revil A., Finizola A., Sortino F. & Ripepe M., 2004b. Geophysical investigations at Stromboli volcano, Italy. Implications for ground water flow and paroxysmal activity, *Geophys. J. Int.*, **157**, 426–440.

Revil, A. *et al*., 2008. Inner structure of La Fossa di Vulcano (Vulcano Island, southern Tyrrhenian Sea, Italy) revealed by high resolution electric resistivity tomography coupled with self-potential, temperature, and soil CO_2 diffuse degassing measurements, *J. geophys. Res.*, **113**, B07207, doi:10.1029/2007JB005394.

Revil, A., Johnson, T. C. & Finizola, A., 2010. Three-dimensional resistivity tomography of Vulcan's forge, Vulcano Island, southern Italy, *Geophys. Res. Lett.*, **37**, L15308, doi:10.1029/2010GL043983.

Richards, K., Revil, A., Henderson, F., Batzle, M. & Haas, A., 2010. Pattern of shallow ground water flow at Mount Princeton Hot Springs, Colorado, using geoelectrical methods, *J. Volc. Geotherm. Res.*, **198**, 217–232.

Romagnoli, C., Casalbore, D., Chiocci, F.L. & Bosman, A., 2009a. Offshore evidence of large-scale lateral collapses on the eastern flank of Stromboli, Italy, due to structurally-controlled, bilateral flank instability, *Mar. Geol.*, **262**, 1–13, doi:10.1016/j.margeo.2009.02.004.

Romagnoli, C., Kokelaar, P., Casalbore, D. & Chiocci, F.L., 2009b. Lateral collapses and active sedimentary processes on the northwestern flank of Stromboli volcano, Italy, *Mar. Geol.*, **265**, 101–119.

Rosi, M., 1980. The Island of Stromboli, *Rend. Soc. It. Miner. Petrol.*, **36**, 345–368.

Segre, A.G., 1968. Notizie sulla morfologia submarina di Stromboli, *Stromboli*, **11**, 45–49.

Sinclair, A.J., 1974. Selection of threshold values in geochemical data using probability graphs, *J. Geochem. Explor.*, **3**, 129–149.

Tibaldi, A., 2001. Multiple sector collapses at Stromboli volcano, Italy: how they work, *Bull. Vulcanol.*, **63**, 112–125.

Tinti, S., Bortolucci, E. & Romagnoli, C., 1999. Modeling a possible Holocenic landslide-induced tsunami at Stromboli volcano. Italy, *Phys. Chem. Earth*, **24**(5), 423–429.

Tinti, S., Bortolucci, E. & Romagnoli, C., 2000. Computer simulations of tsunamis due to sector collapse at Stromboli. Italy, *J. Volc. Geotherm. Res.*, **96**, 103–128.

Tinti, S., Pagnoni, G., Zaniboni, F. & Bortolucci, E., 2003. Tsunami generation in Stromboli island and impact on the south-east Tyrrhenian coasts, *Nat. Hazards Earth Syst. Sci.*, **3**, 299–309.

Tinti, S., Maramai, A.,·Armigliato, A., Grazian,i L., Manucci, A., Pagnoni, G. & Zaniboni, F. 2006. Observations of physical effects from tsunamis of December 30, 2002 at Stromboli volcano, southern Italy, *Bull. Volcanol.*, **68**, 450–461, doi:10.1007/s00445–005-0021-x.

Tinti, S., Zaniboni, F., Pagnoni, G. & Manucci A., 2008. Stromboli Island (Italy): Scenarios of Tsunamis Generated by Submarine Landslides, *Pure appl. geophys.*, **165**, 2143–2167, doi:10.1007/s00024–008-0420-y.

Waxman, M.H. & Smits, L.J.M., 1968. Electrical conductivities in oil bearing shaly sands, *Soc. Pet. Eng. J.*, **8**, 107–122.

Weinstein, Y., 2007. A transition from strombolian to phreatomagnatic activity induced by a lava flow damming water in a valley, *J. Volc. Geotherm. Res*, **159**(1–3), 267–284.